Proper generalized decomposition for parameterized Helmholtz problems in heterogeneous and unbounded domains: application to harbor agitation

David Modesto, Sergio Zlotnik and Antonio Huerta*

Laboratori de Càlcul Numèric (LaCàN), E.T.S. Ingenieros de Caminos, Universitat Politècnica de Catalunya, BarcelonaTech, 08034 Barcelona, Spain.

Abstract

Solving the Helmholtz equation for a large number of input data in an heterogeneous media and unbounded domain still represents a challenge. This is due to the particular nature of the Helmholtz operator and the sensibility of the solution to small variations of the data. Here a reduced order model is used to determine the scattered solution everywhere in the domain for any incoming wave direction and frequency. Moreover, this is applied to a real engineering problem: water agitation inside real harbors for low to mid-high frequencies.

The Proper Generalized Decomposition (PGD) model reduction approach is used to obtain a separable representation of the solution at any point and for any incoming wave direction and frequency. Here, its applicability to such a problem is discussed and demonstrated. More precisely, the contributions of the paper include the PGD implementation into a Perfectly Matched Layer framework to model the unbounded domain, and the separability of

*Corresponding author

Email address: {david.modesto,sergio.zlotnik,antonio.huerta}@upc.edu (David Modesto, Sergio Zlotnik and Antonio Huerta)

URL: http://www.lacan.upc.edu (David Modesto, Sergio Zlotnik and Antonio Huerta)

the operator which is addressed here using an efficient higher-order projection scheme.

Then, the performance of the PGD in this framework is discussed and improved using the higher-order projection and a Petrov-Galerkin approach to construct the separated basis. Moreover, the efficiency of the higher-order projection scheme is demonstrated and compared with the higher-order singular value decomposition.

Keywords: Reduced Order Models, Proper Generalized Decomposition, Helmholtz, Parameterized solutions, wave propagation, harbor

1. Introduction

A large number of models involving the propagation of harmonic waves in unbounded domains are governed by Helmholtz-type partial differential equations. Their numerical solution is usually computationally demanding. Well-known difficulties are: pollution errors [1–3], treatment of the unbounded domain [4], and modeling small geometric features that have a large influence on the scattered field [5, 6]. Moreover, in engineering practice, wave propagation computations are usually one of many steps in a design process, an optimization strategy or an identification analysis. In summary, accuracy is compromised because the large computer costs drastically reduce the number (or range) of parameters tested. Note that the obvious approach of directly interpolating a few (costly) computed solutions to estimate results for intermediate parameter values is not viable because the solution is extremely sensitive to the parameters (e.g. incoming wave frequency and direction, geometry, etc.).

This paper proposes a strategy to reduce the computational limit imposed on the number of Helmholtz solutions that are feasible to compute in a de-

sign or optimization process. More precisely, the objective is to construct the generalized (high-dimensional) solution of a parameterized scattering problem in an heterogeneous and unbounded domain. This generalized solution, recently called *computational vademecum* [7] in a more general framework, provides the engineer a way to evaluate in real-time any tentative scattering situation (e.g. the Helmholtz solution and its derivatives). Therefore it extremely accelerates the process of evaluating solutions of the Helmholtz problem.

There are several possibilities to parameterize the scattering problem, here the focus is on the parameters defining the incident wave: angular frequency and incoming wave direction. Each of these parameters ranges in a bounded interval (usually application-dependent) and is considered as a new 1D coordinate of the classical Helmholtz equation. This results in a high-dimensional Helmholtz problem whose solution provides the scattered field at any point of the domain and for any incident condition. Moreover, the generalized solution is computed only once whenever it is assumed that the other data (geometry, boundary conditions, etc.) do not change, which is usual in most of engineering applications. The important point is that any subsequent evaluation of the scattered field is readily obtained by means of a fast post-process (this, for instance, can be the case of a time signal including a wide range of frequencies).

The high-dimensional character of the proposed problem involves an exponential growth of degrees of freedom (the so-called *curse of dimensionality*) when using standard mesh-based discretization techniques. A reduced order model can circumvent this critical difficulty, see some previous applications to parameterized Helmholtz equations in [8–12], among others.

Here, the proper generalized decomposition (PGD) [13, 14] is used. This

method has been studied and successfully applied to various problems in computational mechanics, see [15–19]. The interested reader is addressed to [20–22] and the references therein for a survey on different PGD techniques. PGD computes iteratively each term of the approximation using products of functions defined in lower dimensions and induces a separated representation (approximation) of the solution. This reduces the high-dimensional complexity of the original problem. Therefore, it is able to circumvent the curse of dimensionality and provide an approximation of the generalized solution.

As usual in any reduced order technique, two different phases are considered: (i) an offline (computational expensive) phase where all the separated approximations are computed, and (ii) an online phase where the generalized solution is particularized at any desired parameter value (i.e. the online solution). It is important to observe that in contrast to classical a posteriori approaches, like POD [23–25] or reduced basis methods [11, 12, 26], the online phase with PGD only requires to evaluate a linear combination of the separated representation. Thus, the online phase does not need any new solve and the PGD approximation can be computed in real-time for any parameter value.

In the present framework, the separated functions are particularized for a range of intermediate frequencies and incoming wave directions. This also contrasts with previous works in this field; see for instance [27], where an a posteriori reduced model for the homogeneous Helmholtz equation has to be constructed for each intermediate value.

Moreover, the PGD requires neither to precompute any trial solution (i.e. a snapshot) nor to solve a singular value decomposition problem. Note that this last point can even preclude the application of POD-based techniques for the Helmholtz problem where dense spatial discretizations may be necessary.

The contributions in this paper are applicable to any heterogeneous and unbounded problem governed by the Helmholtz equation, and requiring a large number of evaluations of the input data. However the presented work is inspired from an engineering application: the prediction of water agitation inside harbors. Particularly, two harbors located in the Northeast of Spain are used as test cases. Note that the parameterized wave propagation problem becomes in this case 4D: two spatial coordinates, one for frequency and one for the incoming wave direction. Separated representations including the frequency as a dimension are not completely new, see for example [28]. However, in this case real-time evaluation of the PGD solution makes the proposed methodology an exceptional tool for harbor design and study.

Some important points in the development of a PGD solver for the described wave problem require special attention and will be discussed in next Sections. First, the computational domain needs to accurately represent an unbounded physical domain. Here the perfectly matched layers (PML) rationale is, for the first time, adapted and employed in a PGD framework. Second, the wave problem induces non-separable terms in the equations that prevent the standard implementation of the PGD algorithms. A higher-order projection based on the PGD solution of a multidimensional equation is used to construct an optimal separable wave problem. And finally, the non-Hermitian character of the involved operator and the oscillatory nature of the wave field induce serious degradations in the convergence of the standard PGD techniques. Here, an improvement is proposed based on a Petrov-Galerkin approach, originally developed in [21], and on the use of the PGD-projection commented before.

2. Problem statement

The Helmholtz equation in an heterogeneous media and unbounded domain is considered. The application to harbors assumed here imposes the use of the *mild slope equation* (MSE) [29, 30], which describes the motion of sea waves over a slow varying bottom depth, and allows to model the refraction and diffraction for deep and shallow waters. The MSE emanates from the incompressible Navier-Stokes equations (with the hypothesis of non-viscous fluid, small amplitude monochromatic waves and slow varying bottom), and is a common and useful tool for evaluating wave agitation in coastal zone and in harbors. In frequency domain it is written as

$$\boldsymbol{\nabla}\cdot(c\,c_g\boldsymbol{\nabla}u) + k^2 c\,c_g u = 0, \tag{1}$$

over an unbounded 2D domain where $u \in \mathbb{C}$ is the wave surface elevation, $k(h,\omega) \in \mathbb{R}$ is the wavenumber, $h(x,y) \in \mathbb{R}$ is the bathymetry (i.e. mean-water-level-depth), $\omega \in I_\omega \subset \mathbb{R}$ is the angular frequency of the monochromatic incoming wave, $c = \omega/k$ is the phase velocity and $c_g = g[\tanh(kh) + kh\,\mathrm{sech}^2(kh)]/(2\omega)$ is the group velocity, where g is the acceleration of gravity. It is important to note that the wavenumber, k, depends on bathymetry, h, and the frequency, ω, by the so-called nonlinear dispersion relation

$$\omega^2 = kg\tanh(kh), \tag{2}$$

which models the effect of the bathymetry on the wave propagation, that is, the refraction.

Boundary conditions are, on one hand, for reflecting/absorbing boundaries $\Gamma_{\mathtt{R}}$,

$$\boldsymbol{n}\cdot c\,c_g\boldsymbol{\nabla}u - ikc\,c_g\alpha\,u = 0 \text{ on } \Gamma_{\mathtt{R}}, \tag{3}$$

where $i = \sqrt{-1}$ is the imaginary unit, $\boldsymbol{n}$ is the outer unit normal, and $\alpha \in [0,1]$ is the experimental complex transmission coefficient controlling

the reflection/absorption properties of the boundary. This coefficient, also known as the impedance parameter in acoustic problems, is equal to zero on totally reflecting boundaries and to one on perfectly absorbing boundaries. On the other hand, unbounded scattering problems require the so-called Sommerfeld radiation condition

$$\lim_{r\to\infty} \sqrt{r}\Big(\frac{\partial}{\partial r} - ik\Big)(u - u_0) = 0, \tag{4}$$

where r is the radial direction and u_0 the incident wave. This wave is defined on a constant far-field bathymetry h_0 by

$$u_0 = \exp(ik_0 x\cos\theta)\exp(ik_0 y\sin\theta) \in \mathbb{C}, \tag{5}$$

where $\theta \in I_\theta \subset \mathbb{R}$ is the imposed incoming wave direction (data) and k_0 is determined from dispersion relation (2) for $h = h_0$.

Remark 1 (amplitude of incoming wave)**.** *It is important to note that the amplitude of the incoming wave is unitary because the solution can be scaled thanks to the linearity of the problem. In fact, the amplitude of the solution u is called the* amplification factor *because it should be scaled with the actual amplitude of the incoming wave to obtain the actual surface elevation.*

The Sommerfeld radiation condition requires, in practice, the introduction of an artificial boundary and its corresponding boundary condition. Many methods have been proposed in the literature to deal with this situation. Among others, they include infinite elements [31], local non-reflecting boundary conditions (NRBC) [32], Dirichlet to Neumann non-local operators [33, 34] and perfectly matched layers (PML) [35]. All these methods have their advantages and drawbacks, see [36] for an interesting review. Here, the PML is chosen as the far-boundary treatment. This technique has been used with success in many applications, see for instance [37–40]. Moreover,

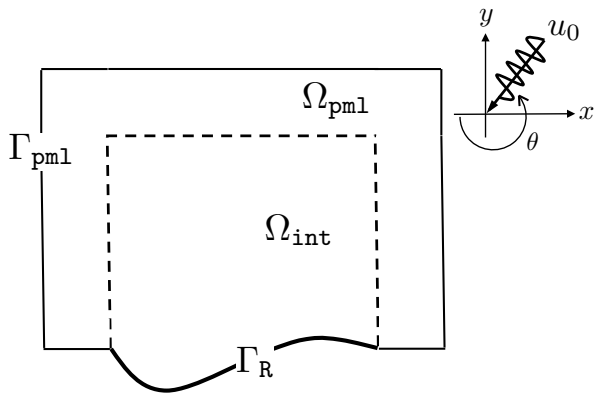

Figure 1: Computational domain sketch.

it provides a straightforward extension to multidimensional models. Finally, note that a first order NRBC is placed on the artificial boundary to minimize spurious reflections.

In this case it is usual to define a bounded computational domain $\Omega = \Omega_{\texttt{int}} \cup \Omega_{\texttt{pml}} \subset \mathbb{R}^2$ union of the region of interest, or interior domain $\Omega_{\texttt{int}}$, and a PML region $\Omega_{\texttt{pml}}$, and to introduce an artificial boundary $\Gamma_{\texttt{PML}}$, see Figure 1. Note that the coefficients c, c_g and k are assumed constant outside the interior domain $\Omega_{\texttt{int}}$, at least in the normal direction to $\Gamma_{\texttt{PML}}$. The Perfectly Matched Layer (PML) surrounds $\Omega_{\texttt{int}}$ in order to absorb outgoing waves. The problem to be solved is then

$$\boldsymbol{\nabla}\cdot(c\,c_g\mathbf{P}\boldsymbol{\nabla}u) + k^2 c\,c_g s_x s_y u = s(x,y,\omega,\theta) \qquad \text{in } \Omega, \tag{6a}$$

$$\boldsymbol{n}\cdot(c\,c_g\mathbf{P}\boldsymbol{\nabla}u) - ikc\,c_g\alpha\,u = 0 \qquad \text{on } \Gamma_{\texttt{R}}, \tag{6b}$$

$$\boldsymbol{n}\cdot(c\,c_g\mathbf{P}\boldsymbol{\nabla}u) - ikc\,c_g u = \boldsymbol{n}\cdot(c\,c_g\mathbf{P}\boldsymbol{\nabla}u_0) - ikc\,c_g u_0 \qquad \text{on } \Gamma_{\texttt{PML}}, \tag{6c}$$

where the non-homogenous term in (6a) is defined as

$$s = \begin{cases} 0 & \text{if } (x,y) \in \Omega_{\texttt{int}}, \\ \boldsymbol{\nabla}\cdot(c\,c_g\mathbf{P}\,\boldsymbol{\nabla}u_0) + k^2 c\,c_g s_x s_y u_0 & \text{if } (x,y) \in \Omega_{\texttt{pml}}, \end{cases} \tag{7}$$

to account for the incident wave and absorb only the scattered waves in the PML region. The diagonal anisotropy matrix defining the absorption in the PML medium, denoted by $\mathbf{P}$, is only different from the identity matrix in the PML area. But it is defined everywhere, as shown in (6), to avoid writing the problem differently in each subdomain. Thus, the boundary condition described by (6b) is identical to (3). The matrix $\mathbf{P}$ is defined as

$$\mathbf{P} = \begin{pmatrix} s_y/s_x & 0 \\ 0 & s_x/s_y \end{pmatrix}, \tag{8}$$

where $s_x = 1 + \sigma_x/\omega$ and $s_y = 1 + \sigma_y/\omega$ are the absorption parameters in the two Cartesian directions. It is important to note, as commented above that $s_x = s_y = 1$ outside the PML region because the absorbing functions $\sigma_x(x) \geq 0$ and $\sigma_y(y) \geq 0$ are zero in $\Omega_{\texttt{int}}$ and monotonic polynomials along the corresponding cartesian absorbing direction. More details on the application of the PML to the Helmholtz equation can be found in [39, 41] among others.

Equation (6c) is a first order non-reflecting boundary condition approximating (4) on $\Gamma_{\texttt{PML}}$, which minimizes non-physical reflections from the PML outer boundary. Thus, $\partial\Omega = \overline{\Gamma}_{\texttt{R}} \cup \overline{\Gamma}_{\texttt{PML}}$ with $\Gamma_{\texttt{R}} \cap \Gamma_{\texttt{PML}} = \emptyset$, and no Dirichlet boundary conditions are imposed.

Remark 2 (separated representations of the coefficients in the equations)**.** *It is important to note that the coefficients in* (6) *are non-constant. In general, they depend on the bathymetry, h (and consequently on the spatial coordinates x and y), the angular frequency of the monochromatic incoming wave, ω, and the incoming wave direction, θ. This dependence is, in general, nonlinear. But the crucial issue for the proposed methodology is that these coefficients are not expressed a priori as separated functions of the coordinates: (x, y), ω, and θ. Thus, they are not written as a sum of products of functions of (x, y), ω, and θ, that is $\sum_{m=1}^{n} F_1^m(x, y)\, F_2^m(\omega)\, F_3^m(\theta)$.*

The method is indeed applicable independently of the separated representation of the data. However, its computational cost increases drastically if this is not the case. Section 5 details the separated representation to approximate these coefficients. In fact, Appendix A formalizes a novel and general strategy to obtain a separable representation of any data.

3. The parameterized wave propagation weak form

For a given geometry and bathymetry, $h(x, y)$, engineers are confronted with multiple evaluations of problem (6) for different values of the angular frequency and direction of the incoming wave, namely ω and θ. As noted in the introduction, knowing the generalized solution of (6) for any ω and θ would drastically improve the performance for both multiple and fast queries. It is important to remark at this point that other parameters can also be included. The absorption coefficient α, see (6b), is a natural candidate to evaluate possible remediation actions in physical boundaries. More challenging implementations can include geometrical parameters, see [42, 43].

Before constructing an approximation to the generalized solution, the multidimensional problem created by considering ω and θ as extra coordinates is formalized. The problem now has four dimensions: two from the computational spatial domain, $(x, y) \in \Omega$, one from the angular frequency, $\omega \in I_\omega$, and one from the incoming wave direction, $\theta \in I_\theta$. Here, I_ω and I_θ denote the corresponding range of interest of both parameters. The total surface elevation, $u(x, y, \omega, \theta)$, is now seen as the four dimensional unknown of the problem. The variational problem equivalent to (6) requires finding $u(x, y, \omega, \theta)$ for all $\delta u(x, y, \omega, \theta)$ in the selected appropriate functional space such that

$$A(u, \delta u) = L(\delta u). \tag{9a}$$

Obviously, this weak form requires an integration over the four-dimensional domain. Thus, the non-Hermitian bilinear form $A(\cdot,\cdot)$ and the linear form $L(\cdot)$ are defined as follows:

$$\begin{cases} A(u,\delta u) = \displaystyle\int_{I_\theta}\int_{I_\omega} a(u,\delta u;\omega)\, d\omega d\theta, \\ L(\delta u) = \displaystyle\int_{I_\theta}\int_{I_\omega} \ell(\delta u;\omega,\theta)\, d\omega d\theta, \end{cases} \tag{9b}$$

where $a(\cdot,\cdot;\omega)$ is the spatial Helmholtz bilinear and continuous form with the parameter dependence explicitly indicated, and, analogously, $\ell(\cdot;\omega,\theta)$ is the spatial Helmholtz linear and bounded functional. They are the classical Helmholtz spatial weak forms, which are dependent on the parameters $(\omega,\theta)\in I_\omega\times I_\theta$, that is

$$a(u,\delta u;\omega) = \big(k^2 c\, c_g s_x s_y u,\delta u\big)_\Omega - \big(c\, c_g \mathbf{P}\boldsymbol{\nabla} u, \boldsymbol{\nabla}\delta u\big)_\Omega + i\alpha\big\langle kc\, c_g u,\delta u\big\rangle_{\Gamma_{\mathtt{R}}} + i\big\langle kc\, c_g u,\delta u\big\rangle_{\Gamma_{\mathtt{pml}}}, \tag{10a}$$

and

$$\ell(\delta u;\omega,\theta) = \big(s,\delta u\big)_\Omega + \big\langle \boldsymbol{n}\cdot(c\, c_g \mathbf{P}\boldsymbol{\nabla} u_0) - ikc\, c_g u_0,\delta u\big\rangle_{\Gamma_{\mathtt{pml}}}. \tag{10b}$$

In the previous and the following equations, $\big(\cdot,\cdot\big)_D$ denotes the $\mathcal{L}^2$ scalar product (for complex functions) in any domain D, while $\big\langle\cdot,\cdot\big\rangle_B$ also denotes the $\mathcal{L}^2$ scalar product of the traces over B.

4. The proper generalized decomposition method (PGD)

Helmholtz problems require fine discretizations of the spatial domain. Moreover, for low-order approximations dense meshes must be enhanced with stabilized formulations to control dispersion errors [44–46]. In spite of the improved efficiency of high-order approximations [47, 48] a large number of degrees of freedom (DOF) is nonetheless required. For instance, as shown in

[47], 10^5 DOF are necessary to attain one significant digit of accuracy with fifth-order finite elements in this MSE problem. Hence, applying a standard discretization technique to solve the 4D problem may easily require here 10^9 DOF when 100 nodes are used for parameters θ and ω. However, PGD may effectively approximate the solution of problem (9) with a 2D computational cost.

PGD imposes an approximation of the wave field $u(x, y, \omega, \theta)$ in a rank-n separated representation, namely

$$u(x, y, \omega, \theta) \approx u^n(x, y, \omega, \theta) = \sum_{m=1}^{n} F_1^m(x, y) F_2^m(\omega) F_3^m(\theta). \tag{11}$$

The PGD approach has to determine the number of necessary terms n, see [49], and the unknown separated functions F_1^m, F_2^m and F_3^m for $m = 1, \ldots, n$. There are several alternatives. Each term m is evaluated sequentially by means of a greedy algorithm

$$u^n(x, y, \omega, \theta) = u^{n-1}(x, y, \omega, \theta) + F_1(x, y) F_2(\omega) F_3(\theta), \tag{12}$$

where u^{n-1} is assumed to be known, and F_1, F_2 and F_3 denote the separated functions of the unknown term (the superscript is dropped for the last term in order to alleviate notation). Substituting (12) in (9a) the following problem must be solved:

$$A(F_1 F_2 F_3, \delta u) = L(\delta u) - A(u^{n-1}, \delta u). \tag{13}$$

Note that this represents a nonlinear problem for the unknowns F_1, F_2 and F_3.

A number of PGD approaches based on linearization techniques have been developed to solve the Eq. (13) efficiently, see for instance [21, 22]. Two of these approaches, which will be compared in Section 6, are detailed next.

4.1. Standard PGD

Consider the test functions δu in Eq. (13) to be separated as

$$\delta u = \delta F_1\, F_2 F_3 + F_1\, \delta F_2\, F_3 + F_1 F_2\, \delta F_3. \tag{14}$$

This expression allows to approximate the solution with an alternating direction strategy (fixed point iteration). Each iteration requires to perform as many sequential steps as separated functions are used to approximate u. Here, the following three stages are iterated until convergence or a proxy for termination is reached (further commented in Section 6):

1. Assume that F_2 and F_3 are known ($\delta F_2 = \delta F_3 = 0$). Compute the linear problem to determine $F_1 \in \mathcal{H}^1(\Omega)$, for all $\delta F_1 \in \mathcal{H}^1(\Omega)$ satisfying

$$A(F_1 F_2 F_3, \delta F_1\, F_2 F_3) = L(\delta F_1\, F_2 F_3) - A(u^{n-1}, \delta F_1\, F_2 F_3). \tag{15a}$$

   Note that this step has a 2D cost. After solving (15a) the function F_1 is $\mathcal{L}^2$ normalized.

2. Assume now that F_1 and F_3 are known ($\delta F_1 = \delta F_3 = 0$). In fact, the solution of the previous step is used here in a Gauss-Seidel strategy. Solve a linear 1D problem to evaluate $F_2 \in \mathcal{L}^2(I_\omega)$, for all $\delta F_2 \in \mathcal{L}^2(I_\omega)$ satisfying

$$A(F_1 F_2 F_3, F_1\, \delta F_2\, F_3) = L(F_1\, \delta F_2\, F_3) - A(u^{n-1}, F_1\, \delta F_2\, F_3). \tag{15b}$$

   After solving (15b) the function F_2 is $\mathcal{L}^2$ normalized.

3. Assume that F_1 and F_2 are known ($\delta F_1 = \delta F_2 = 0$) from the two previous steps. The separated function in the incoming direction domain, $F_3 \in \mathcal{L}^2(I_\theta)$, is found for all $\delta F_3 \in \mathcal{L}^2(I_\theta)$ as the solution of

$$A(F_1 F_2 F_3, F_1 F_2\, \delta F_3) = L(F_1 F_2\, \delta F_3) - A(u^{n-1}, F_1 F_2\, \delta F_3). \tag{15c}$$

This iterative scheme is required at each enrichment step in Eq. (12). Note that the 4D nature of the original problem is reduced to the iteration of one 2D problem (15a) and two 1D problems (algebraic equations 15b and 15c). Consequently, the computational cost associated to the PGD approximation is the product of three factors: (i) the cost of the 2D Helmholtz solver, (ii) the total number of iterations performed and (iii) the number of terms involved in the separable representation of u. For the majority of elliptic problems, both, the number of iterations and the required terms are sufficiently small to ensure computational savings of several orders of magnitude, see for instance [14].

Unfortunately, the optimality of the standard approach is critically degraded for non-symmetric operators, see [21]. This issue also applies to the non-Hermitian MSE problem. Moreover, its complexity is increased due to the oscillatory nature of the solution. As shown in Section 6 the standard approach is, in general, not converging. The offline PGD constructor is imposed by a non-standard rationale introduced next.

Remark 3 (Algebraic equations)**.** *Note that steps 2 and 3, associated respectively to ω and θ, can be solved pointwise because they are algebraic equations. That is, no derivatives with respect to ω or θ exist in the strong form of the problem, see* (6)*. Since the choice of these sampling points is not trivial, here an approximation spaces for $F_2(\omega)$ and $F_3(\theta)$ are a priori defined for the weak form strategy in order to retain, when possible, a* best approximation *strategy over the whole range of the parameters.*

4.2. Petrov-Galerkin PGD

The Petrov-Galerkin PGD (PG PGD) is proposed in [21] and is applied here to recover the convergence of the PGD solution. Let us substitute the

test functions δu in Eq. (13) by $\delta\tilde{u}$, that is

$$A(F_1F_2F_3, \delta\tilde{u}) = L(\delta\tilde{u}) - A(u^{n-1}, \delta\tilde{u}), \tag{16}$$

where $\delta\tilde{u}$ is defined by

$$\delta\tilde{u} = \delta\widetilde{F}_1\,\widetilde{F}_2\widetilde{F}_3 + \widetilde{F}_1\,\delta\widetilde{F}_2\,\widetilde{F}_3 + \widetilde{F}_1\widetilde{F}_2\,\delta\widetilde{F}_3.$$

Functions $\widetilde{F}_1(x, y)$, $\widetilde{F}_2(\omega)$ and $\widetilde{F}_3(\theta)$ are obtained by solving the auxiliary problem

$$A(\delta u, \widetilde{F}_1\widetilde{F}_2\widetilde{F}_3) = \big(\delta u, F_1F_2F_3\big)_{\Omega\times I_\omega\times I_\theta}, \tag{17}$$

for all δu in the form of Eq. (14).

This is a Petrov-Galerkin approach because the space of the test functions does not coincide with the space of trial functions as clearly see in (16). In fact, (17) defines the space of test functions. Note that this new space is defined such that its product, using $A(\cdot,\cdot)$, by functions of the trial space is equal to the $\mathcal{L}^2$ product of functions of the trial space. In a sense tying to bring the optimal properties of the $\mathcal{L}^2$ product to $A(\cdot,\cdot)$. For this reason this algorithm was originally developed for non-symmetric convective-dominated problems with space-time decompositions, see [21]. In general, this approach can be advantageous for problems whose behavior is not sufficiently similar to the optimal case as provided by the $\mathcal{L}^2$ norm. Note that the implementation of PG PGD is a natural choice here since the MSE problem is non-Hermitian. Numerical examples of Section 6 show that this approach is able to provide solutions in cases where the standard one fails.

Equations (16) and (17) are separable and therefore can be approximated using the same fixed point algorithm described before. Similarly to the standard PGD algorithm (15), the PG PGD approach requires solving a three stage procedure. In this case, however, each stage involves the solution of two

equations: one to evaluate $\widetilde{F}_i$ and one to evaluate F_i, $i = 1, 2, 3$. Note that each pair of equations induce the same matrix and therefore the computational cost is not duplicated. After convergence of the fixed point algorithm, the auxiliary functions $\widetilde{F}_1$, $\widetilde{F}_2$ and $\widetilde{F}_3$ are not longer necessary.

Remark 4 (convergence of PGD algorithms)**.** *For pure diffusive elliptic problems, the number of iterations in the fixed point algorithm typically does not exceed ten before the convergence criterion is fulfilled [13]. For more complex frameworks, like the one proposed here, the new term $F_1F_2F_3$ may not converge and a maximum number of iterations is usually imposed. For the present problem it has been observed that, if the maximum number of iterations is reduced, for instance to three, the PGD approximation may require more terms (more "modes") but the overall computational cost is drastically reduced.*

5. Separability of the MSE

PGD requires the operators $A(\cdot,\cdot)$ and $L(\cdot)$, see Eqs. (9) and (10), to be expressed in a separable form. Otherwise, the integration of the weak form needs to be done in the full multidimensional space and this requires an exponential number of operations. Note that this does not preclude the applicability of the method, but extremely penalizes the computations done in the offline phase. The separability of these operators is determined by the separability of the involved functions, namely: i) incident wave (5), ii) bathymetry coefficients, see Remark 2, and iii) PML coefficients appearing in matrix $\mathbf{P}$ (8).

Separated approximations of these functions are determined as a preprocess of the PGD algorithm. Several options can be used, for instance the popular singular value decomposition or its higher-order extensions [50]

or the empirical interpolation method [51]. Here, however, an alternative procedure is proposed. It is called higher-order PGD-projection and it is formalized in Appendix A.

the PGD-projection provides an optimal decomposition, which coincide with the POD, when separated representations only involve two parameters. Moreover, in large problems PGD is better because it avoids the cost associated to an singular value decomposition (SVD) problem.

This projection is particularly useful to reduce the rank of already separated representations as will be shown in the next Section. All the advantages of higher-order PGD-projection are discussed and demonstrated in Appendix A with several examples.

5.1. Getting separated representations of the coefficients

The separable version of the operator $A(\cdot,\cdot)$ is obtained by means of separable versions of the coefficients b_i defined as follows,

$$a(u,\delta u;\omega) = \big(\overbrace{k^2 c\, c_g}^{b_1} s_x s_y u, \delta u\big)_\Omega - \big(\overbrace{c\, c_g}^{b_2} \mathbf{P}\boldsymbol{\nabla} u, \boldsymbol{\nabla}\delta u\big)_\Omega + i\alpha\big\langle \underbrace{kc\, c_g}_{b_3} u, \delta u\big\rangle_{\Gamma_{\mathtt{R}}} + i\big\langle \underbrace{kc\, c_g}_{b_3} u, \delta u\big\rangle_{\Gamma_{\mathtt{pml}}}. \quad (18)$$

The functions $1/s_x$ and $1/s_y$ that appear in $\mathbf{P}$, recall (8), need also a separable representation. Note that $s_x(x,\omega) = 1+\sigma_x(x)/\omega$ and $s_y(y,\omega) = 1+\sigma_y(y)/\omega$ are already separable.

By means of the PGD-projection proposed in Appendix A an optimal rank-s_i separated representation of coefficient b_i for $i = 1,2,3$ is computed

$$\mathcal{P}^{\mathtt{pgd}}\big[b_i(h,\omega)\big] = \sum_{m=1}^{s_i} \beta_i^m B_{i,1}^m(h) B_{i,2}^m(\omega). \quad (19)$$

This representation uses normalized functions $B_{i,1}^m$ and $B_{i,2}^m$ and, consequently, β_i^m provides information on the amplitude of term m. For instance, Figure

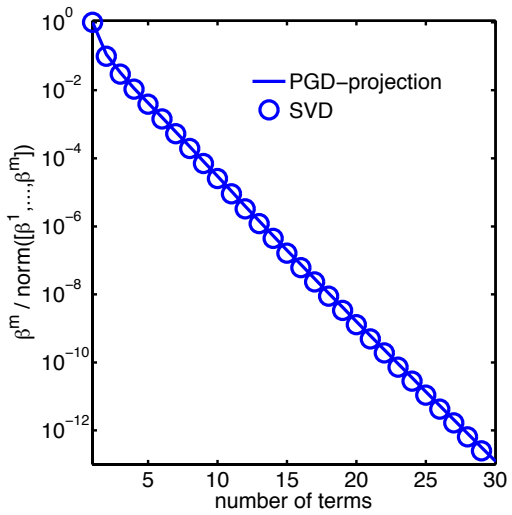

Figure 2: Normalized coefficients ($\log_{10}$ scale) for the PGD-projection and SVD of $b_1(h,\omega)$. The range for the bathymetry and frequency are $h \in [1, 65]$ and $\omega \in [0.4, 2]$, both discretized with 1000 equidistant nodes.

2 depicts for coefficient b_1 the normalized coefficients $\beta_1^m / \left\|[\beta_1^1, \ldots, \beta_1^m]\right\|_2$ for $m = 1, \ldots, 30$. The range of bathymetry and frequency cover the range of realistic values on the Mediterranean coast. Only 20 terms are required to generate a very accurate separable structure. Similar results are observed for the other coefficients b_2 and b_3.

The PGD-projection is also used to generate optimal separated representations for $1/s_x(x,\omega)$ and $1/s_y(y,\omega)$. The resulting expressions are analogous to (19) but with products of functions depending on x (or y) in the first function and ω for the second one.

5.2. Getting separable incident wave

Once the separability of the bilinear form $A(\cdot,\cdot)$ is achieved, the linear functional $L(\cdot)$ is also separated provided a separable form of the incident wave, see Eq. (10b), is obtained.

In contrast to the expression of the MSE coefficients, the incident wave

$u_0(x, y, \omega, \theta)$ depends on every parameter. Thus, an optimal decomposition is defined as

$$\pi^{\texttt{pgd}}\big[u_0(x, y, \omega, \theta)\big] = \sum_{m=1}^{q} \beta_0^m B_{0,1}^m(x, y) B_{0,2}^m(\omega, \theta), \tag{20}$$

that separates $(x, y) \in \Omega_{\texttt{pml}}$ from the 2D parametric coordinate $(\omega, \theta) \in I_\omega \times I_\theta$. The cost of this projection is superior to the previous coefficients. Nevertheless, it is still affordable for small PML domains. Thanks to the spatially separated structure of u_0, recall Eq. (5), the expression (20) can be constructed as the product of: (i) the projection of $\exp(ik_0 x \cos\theta)$ (1D in x), and (ii) the projection of $\exp(ik_0 y \sin\theta)$ (1D in y). An example of these projections is shown in Appendix A.2. This procedure drastically reduces the cost for large PML domains.

Remark 5 (practical computation of projections)**.** *Note that all the projections presented here, that separate both, coefficients and incident wave, can be computed in a proper reference domain and then mapped to the real coordinates. This reference domain must include all the possible combinations of the parameter values that are required in practice. Thus, there is no need to compute a new projection every time the bathymetry and the PML domain are modified.*

6. Application examples

This section presents three problems: one academic example and two engineering applications related to harbor design. All problems are governed by the MSE (6) in an unbounded domain where the PML technique is applied in the outer boundary. The performance of the proposed methodology (in the offline phase) depends on the selected range of parameters; that is, on the intervals I_ω and I_θ. In the academic example, for demonstration purposes,

these intervals cover from low to high frequencies for any fixed incoming wave direction. For both engineering applications realistic values are chosen and the range frequencies and incoming wave directions studied are related to the observed incoming waves in the region.

Before presenting the example in detail a few general remarks are pertinent. First, note that in order to ensure a correct absorption of the scattered waves, the width of the rectangular PML domain, namely $L_{\texttt{pml}}$, is set as 1.5 times the maximum wave length induced by the lower frequency in each example [37]. Functions $s_x = 1 + \sigma_x/\omega$ and $s_y = 1 + \sigma_y/\omega$, which quantify the absorption of the scattered wave, are defined using a second order polynomial

$$\sigma_x(x) = \sigma_{\texttt{max}}\big[(x - x_0)/L_{\texttt{pml}}\big]^2, \tag{21}$$

and analogously for $\sigma_y(y)$, where x_0 (respectively y_0) stands for the coordinate value at which the interface boundary $\Omega_{\texttt{int}} \cap \Omega_{\texttt{pml}}$ is placed. The maximum absorption $\sigma_{\texttt{max}}$ is then set in order to maximize the damping of the scattered wave using the values proposed in [52]. Note that Eq. (21) is a particular standard choice of the PML absorption that usually provides sufficient accuracy. More definitions can be used, like the unbounded damping function [53].

Second, convergence criteria must be imposed. For the fixed point algorithms, see Eq. (15), convergence is assumed when

$$\frac{\left\| \prod_{i=1}^{3} F_i^{(\nu)} - \prod_{i=1}^{3} F_i^{(\nu-1)} \right\|^2_{\mathcal{L}^2(\Omega \times I_\omega \times I_\theta)}}{\left\| \prod_{i=1}^{3} F_i^{(\nu)} \right\|^2_{\mathcal{L}^2(\Omega \times I_\omega \times I_\theta)}} < \varepsilon^2,$$

where ν stands for the nonlinear iteration counter (analogously for the auxiliary functions $\widetilde{F}_i$ of the PG PGD algorithm).

For the greedy procedure (the number of terms involved in the PGD solution) the stopping criteria is based on the contribution of the last term,

namely

$$\frac{\|F_1F_2F_3\|^2_{\mathcal{L}^2(\Omega\times I_\omega\times I_\theta)}}{\|u^{n-1}\|^2_{\mathcal{L}^2(\Omega\times I_\omega\times I_\theta)}} < \varepsilon^2. \tag{22}$$

The condition (22) is straightforward to evaluate, it does not imply costly calculations and usually gives valid estimations for low tolerances (for instance $\varepsilon \leq 10^{-6}$). More accurate (and costly) criteria can be used to stop the enrichment procedure, for example using a goal-oriented strategy based on the solution of an adjoint problem, see [49].

A third point is how to evaluate the accuracy of the approximation provided by the PGD strategy. Here, two quantities of interest (QoI) related to harbor design are used. One is the wave height $H(x, y, \omega, \theta) = |u(x, y, \omega, \theta)|$, recall Remark 1. Other is the maximum wave height in an area of interest $\mathcal{A} \subset \Omega_{\texttt{int}}$ of the interior domain, that is

$$H_{\texttt{max}}(\omega, \theta) = \max_{(x,y)\in\mathcal{A}} H(x, y, \omega, \theta).$$

Based on these QoI, two error measures are defined: i) the normalized spatially-averaged error of the wave height at some design parameter values ω^* and θ^*,

$$\frac{\|H^n(x, y, \omega^*, \theta^*) - H(x, y, \omega^*, \theta^*)\|_{\mathcal{L}^2(\mathcal{A})}}{\|H(x, y, \omega^*, \theta^*)\|_{\mathcal{L}^2(\mathcal{A})}}, \tag{23a}$$

and ii) the normalized parametrically-averaged error of the maximum wave height,

$$\frac{\|H^n_{\texttt{max}}(\omega, \theta) - H_{\texttt{max}}(\omega, \theta)\|_{\mathcal{L}^2(I_\omega\times I_\theta)}}{\|H_{\texttt{max}}(\omega, \theta)\|_{\mathcal{L}^2(I_\omega\times I_\theta)}}. \tag{23b}$$

The quantities H^n and $H^n_{\texttt{max}}$ are the measures based on the rank-n PGD solution, while H and $H_{\texttt{max}}$ are based on a reference solution obtained numerically.

The fourth and last point concerns the numerical discretization. All the examples use standard continuous Galerkin finite elements. More precisely,

the spatial meshes use fourth order simplices with a minimum wave resolution of 8 nodes per wavelength. Parametric meshes are all linear with a Chebyshev nodes.

6.1. Scattering on a cylindrical obstacle

The first example is a standard benchmark for scattering problems. It consists in a totally reflecting scatterer with radius $R = 1$. The solution is parametrized in space and frequency, $u(x, y, \omega)$, leaving the incident angle fixed at value $\theta = 3\pi/2$. The 3D PGD approximation is then given by

$$u(x, y, \omega) \approx u^n(x, y, \omega) = \sum_{m=1}^{n} F_1^m(x, y) F_2^m(\omega). \tag{24}$$

Three different solutions are computed for three frequency regimes. Low frequencies: $I_\omega = [6.28, 10.47]$, medium: $I_\omega = [6.28, 22.15]$ and high frequencies: $I_\omega = [6.28, 31.45]$, with a minimum dimensionless wavenumber $kR = 1$, and a maximum $kR = \{13, 50, 100\}$, respectively, on the cylindrical obstacle. In this first example a maximum number of 3 nonlinear iterations per term is used, recall Remark 4. The spatial domain, bathymetry and boundary conditions are shown in Figure 3 as well as the wave height field generated for the particular case $kR = 99$. The fourth order spatial mesh has $\approx 4 \times 10^5$ nodes for the high frequency case, whereas the parametric domains, I_ω, are discretized with an overkilled mesh of 1000 nodes.

Left panel of Figure 4 depicts the contribution of the last term, see Eq. (22), for the three solutions corresponding to the three frequency ranges. Only the PG PGD algorithm is depicted in this case. A strong influence on the convergence rate is observed when increasing the frequency range, being in agreement with previous applications of reduced modeling for scattering problems [11, 12]. Moreover, note that convergence exhibits oscillations that tend to grow as the frequency range increases. This effect is largely amplified

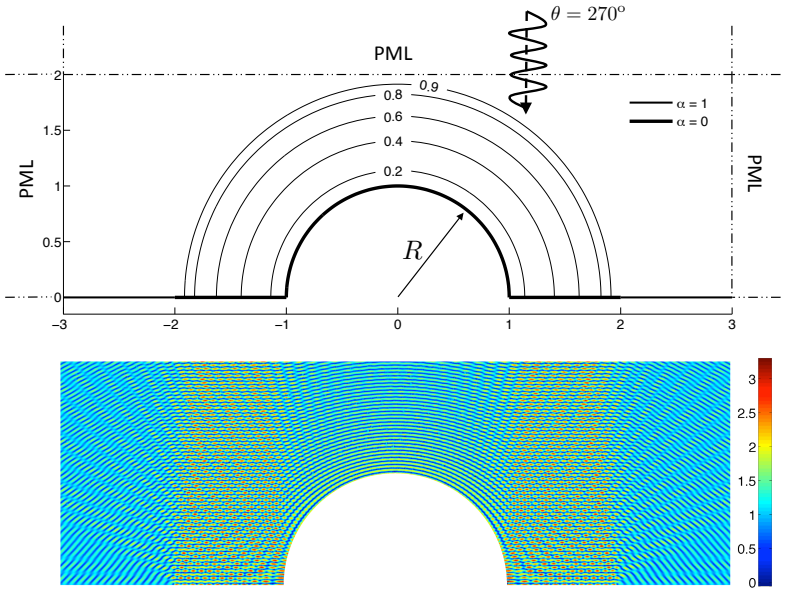

Figure 3: Cylindrical scattering: problem statement. Spatial domain with values of the absorbing coefficient α on the boundary and contour lines of the bathymetry (top). Wave-height for a fixed frequency $\omega^* = 31.16$rad/s (bottom).

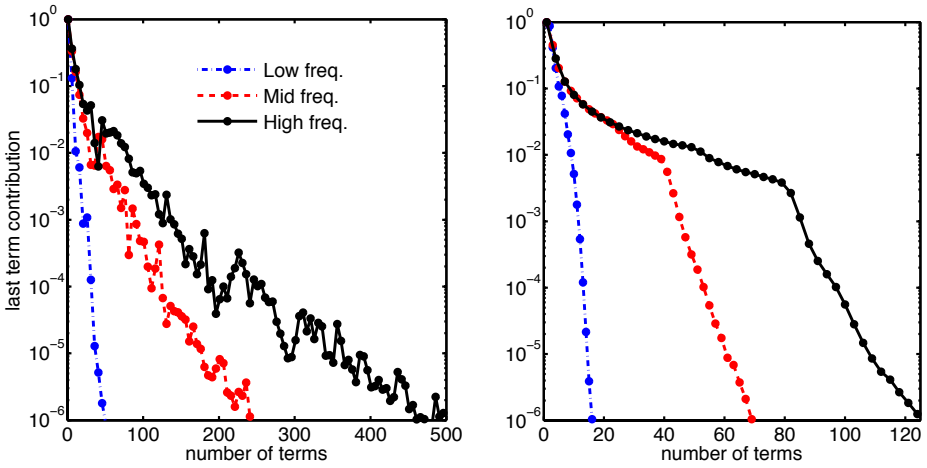

Figure 4: Cylindrical scattering: contribution of the last mode to the PG PGD (left) and its corresponding PGD-projection (right) for three different frequency ranges from low (maximum $kR = 13$) to high (maximum $kR = 100$).

when using the standard PGD algorithm to approximate the solutions (not shown). Comparison of PGD algorithms is further presented for this example in terms of accuracy.

The right panel of Figure 4 shows the PGD-projected version of the three solutions. The PGD-projection procedure is equivalent to POD for two separated dimensions. The obtained solutions, therefore, are optimal in the number of terms (compare the x-axis of left and right panels of Figure 4). In addition the projected solutions present a monotone convergence. Note that, in this case, the PGD-projection is applied to a function, which is already expressed as a separated representation. Therefore, the computational cost to reduce the representation to the relevant modes is almost negligible compared with the PG PGD offline solution, see Appendix A. In addition, the large reduction in the number of terms (modes) contributes to reduce the time and memory required in the online phase.

The accuracy of (24) is studied, for a given frequency, using the first QoI-based error (23a). The area of interest in this case is the complete interior spatial domain. Three convergence curves are shown at each panel of Figure 5 corresponding to the online solutions given by the standard PGD algorithm, PG PGD and the PGD-projection. Recall that these errors are computed with real-time evaluations of the PGD. All depicted curves use fixed frequency values, namely ω^* in Figure 5, which do not coincide with the discretization of the parametric domain I_ω. Note that results show a similar trend to that observed in the last term contribution of Figure 4: the larger the frequency ranges, the more terms are needed to obtain similar accuracy. Furthermore, small variations in frequency present in some cases very different convergence curves, as seen comparing the top and bottom rows of Figure 5. This variation in convergence curves is not present in the

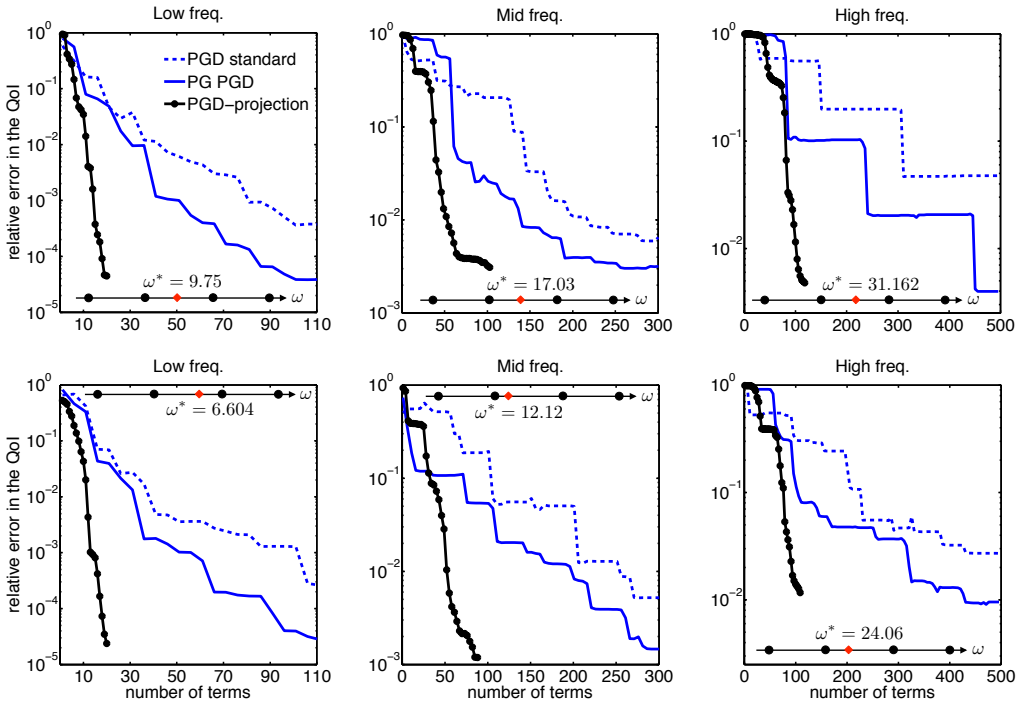

Figure 5: Cylindrical scattering: convergence of relative error of wave-height in the interior domain at a fixed frequency ω^*, see Eq. (23a), versus number of modes. Plots depict three PGD strategies (PG PGD, standard and projection) for three frequencies ranges: low (left), medium (middle) and high (right). The relative position of value ω^* within the 1D range is highlighted by a red rhombus marker.

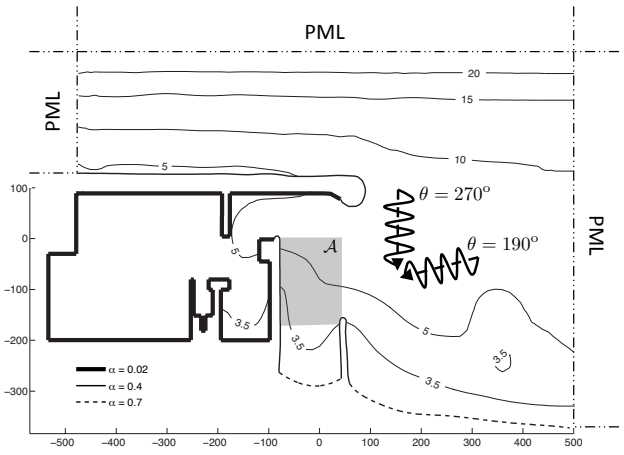

Figure 6: Mataró harbor: problem statement. Spatial domain with values of the absorbing coefficient α on the boundary and bathymetry. The area $\mathcal{A} \subset \Omega_{\texttt{int}}$ of interest is highlighted. The range of variability of the incoming wave direction is also illustrated.

solutions provided by the PGD-projection.

Finally, it can be observed that, despite in this simple test the standard PGD algorithm converges, the PG PGD exhibits a better convergence.

6.2. Mataró harbor

The second example corresponds to a study of the water agitation in Mataró harbor, located North of Barcelona (Spain). In this case the realistic harbor geometry largely increases the number of reflected waves, increasing the difficulty of the computational problem. The computational domain, bathymetry and boundary conditions are shown in Figure 6. The area of interest $\mathcal{A} \subset \Omega_{\texttt{int}}$ defining the error measure (23) is also shown in Figure 6. It corresponds to the wave impact region on the inlet channel of the harbor.

The solution in this case is fully parameterized with space, frequency and incoming direction, i.e. $u(x, y, \omega, \theta)$. Its PGD approximation, u^n, is separated

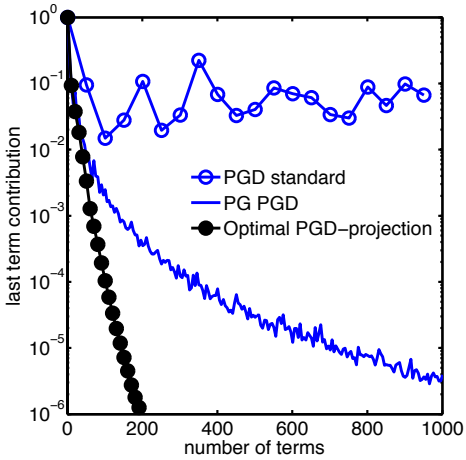

Figure 7: Mataró harbor: contribution of the last term to the standard PGD, PG PGD, and PGD-projected solution.

in the form of Eq. (11). Incident waves are in accordance with those observed offshore in the region: $\omega \in [0.39, 0.63]$ (from 10s to 16s of wave period) and $\theta \in [1.05\pi, 3\pi/2]$. The discretization used is $15\,757 \times 50 \times 50$ nodes for (x, y), ω and θ respectively. Using the notation introduced in Appendix A, the rank-q projection of the PGD solution u^n is computed here as

$$u_\pi^q(x, y, \omega, \theta) = \pi^{\texttt{pgd}}\big[u^n(x, y, \omega, \theta)\big] = \sum_{m=1}^{q} \beta^m F_{\pi,1}^m(x, y) F_{\pi,2}^m(\omega, \theta), \qquad (25)$$

and thus, optimal projections are obtained since u_π^q is separated in two dimensions.

The contribution of the last term is compared in Figure 7 for the PG PGD, the standard PGD and the optimal PGD-projection. Despite this example remains in the low frequency regime, the standard PGD does not converge. In contrast, PG PGD is able to converge, but the number of terms required to reach a certain level of accuracy is far from optimal.

The computational cost of the offline phase is largely determined by the number of spatial problems to be solved (i.e. the number of iterations needed

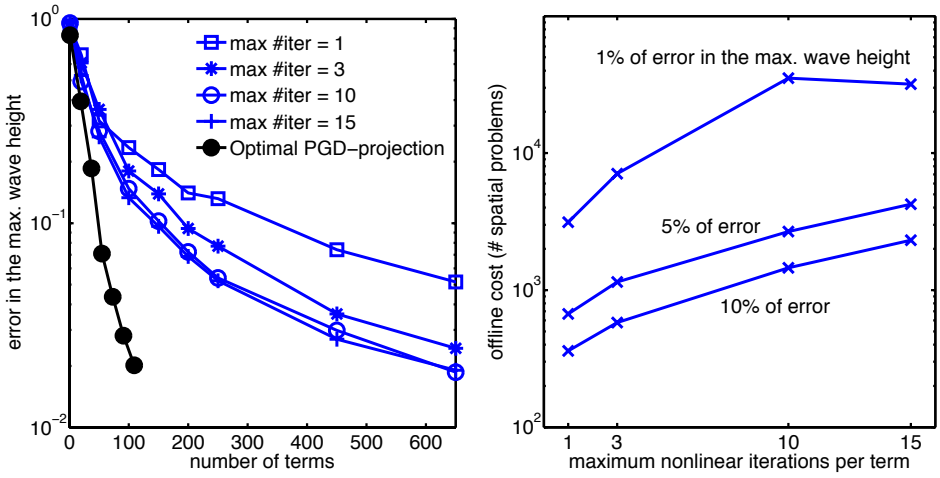

Figure 8: Mataró harbor: analysis of the maximum number of nonlinear PGD iterations $\nu_{\texttt{max}}$. Error of the maximum wave height in the area of interest, see Eq. (23b), versus the number of terms of various PG PGD expansions (left). For fixed values of the error (23b), the required number of 2D problems solved in the PGD construction is shown versus the values of $\nu_{\texttt{max}}$ (right).

for convergence times the required terms). As commented earlier, the maximum number of nonlinear iterations per term, namely $\nu_{\texttt{max}}$, has a direct impact on this cost. Its influence is explored here by solving the same problem for different values of $\nu_{\texttt{max}}$ and measuring the error indicator (23b) in the area $\mathcal{A}$. These tests (left panel of Figure 8) show that $\nu_{\texttt{max}}$ does not improve the quality of the PGD solution significantly. Furthermore, the right panel of the same Figure depicts the offline cost (# spatial problems) to reach a fixed level of error versus the value of $\nu_{\texttt{max}}$. In this case, using the PGD-projected solution provided by the extreme case $\nu_{\texttt{max}} = 1$ gives the better performance in terms of accuracy and also in terms of computational cost.

Finally, a drastic increase on the computational cost is observed to reach an engineering accuracy in those areas where a lot of reflections are involved. This is shown in Figure 9 that depicts the wave amplification for an unfa-

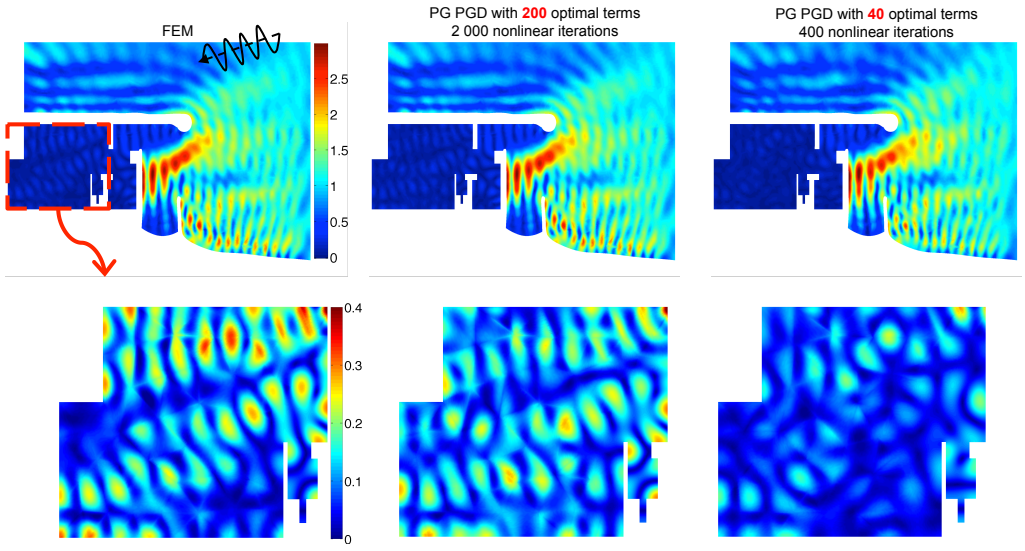

Figure 9: Mataró harbor: wave amplification for the particular case $\omega = 0.61$rad/s and $\theta = 194.5°$. It is shown using spatial FEM (left column), PG PGD with 200 optimal terms (middle column) and PG PGD with 40 optimal terms (right column). The interior area of the harbor is zoomed in the bottom row.

vorable propagation case. The spatial computation with FEM is used as a reference. Despite a good solution is predicted in the exterior harbor region with 40 PGD terms in the expansion, at least 5 times more terms are required to capture the wave physics in the interior (much more reflective area).

6.3. Barcelona harbor

A problem similar to the previous example is solved now for the Barcelona harbor. In this case the geometry is more complex and the size of the harbor is larger, further increasing the number of reflections and therefore making the problem more challenging. The spatial domain, bathymetry and boundary conditions are depicted in Figure 10. The incoming direction $\theta \in [\pi, 3\pi/2]$ is considered, and the frequency range is $\omega \in [0.39, 0.63]$ (same as in the previous example as both locations are close by). Nevertheless, the maximum frequency induces here approximately 90 waves within the domain, moving

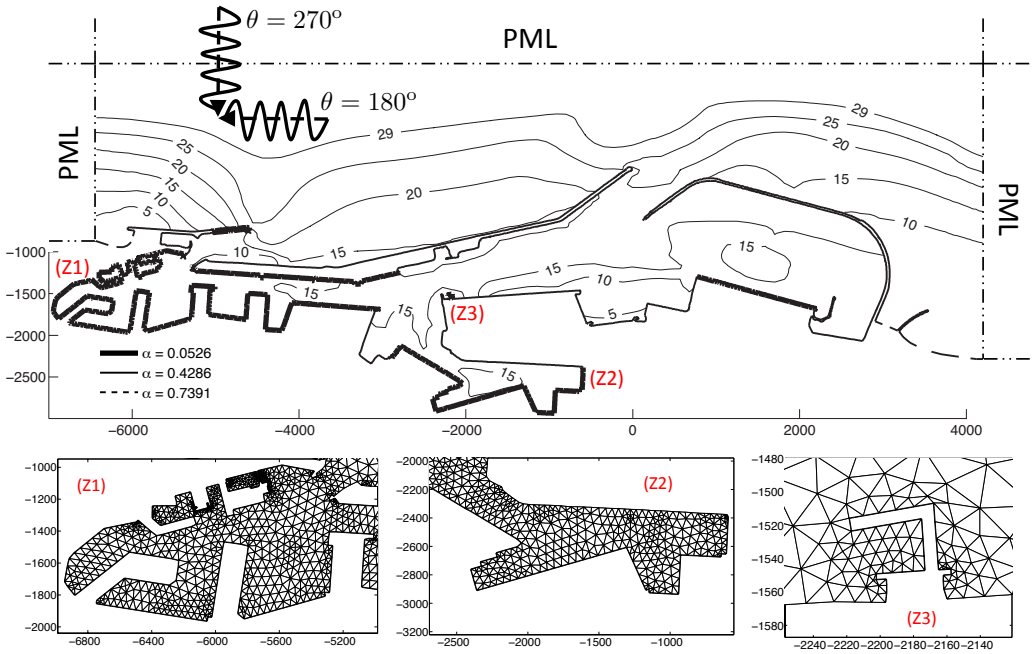

Figure 10: Barcelona harbor: problem statement. Spatial domain with values of the absorbing coefficient α on the boundary, see Eq. (3), and contour lines of the bathymetry. The range of variability of the incoming wave direction is also illustrated. The spatial mesh is shown for three different zooms of the interior domain.

the study from low to medium-high frequency range. The discretization has $2\ 10^5 \times 100 \times 50$ number of nodes for (x, y), ω and θ respectively. Optimal PGD-projected solutions are also computed analogously to Eq. (25).

The Figure 11 depicts the contribution of the last term to the PG PGD and its optimal PGD-projection. Standard PGD is in this case discarded. The convergence of PG PGD is slow, nevertheless, in the first 500 terms it concedes with the optimal curve, showing the proper behavior of the algorithm (these terms provide relevant information) and the inherent complexity of the problem.

The accuracy of the PG PGD is studied in three different areas of interest, see Figure 12. In each area the PGD solution is compared with a reference

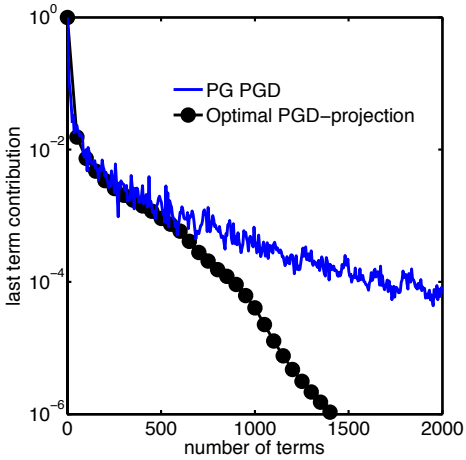

Figure 11: Barcelona harbor: Contribution of the last term ($\log_{10}$ scale) to the PG PGD and to its PGD-projected solution.

one (computed using standard FEM) for a given value of the parameters. Good results, always under engineering accuracy, are observed in all cases and specially for the wave phase.

The PG PGD provided 4015 terms that were later PGD-projected to the 1500 optimal terms shown in the Figure 12. The maximum wave height along the inlet channel of the harbor (left column of the same Figure) is well-captured with less than 10% of error. Same behavior is observed for the inner harbor region (in the middle column). For the more reflective area (right column) the error increases up to the 15%. This corroborates the results of the previous example, where the required terms drastically increase in presence of higher reflections.

7. Concluding remarks

This paper proposes the application of PGD to approximate the 4D generalized solution of the Helmholtz equation in heterogeneous and unbounded domains. The generalization includes variability of some design parameters:

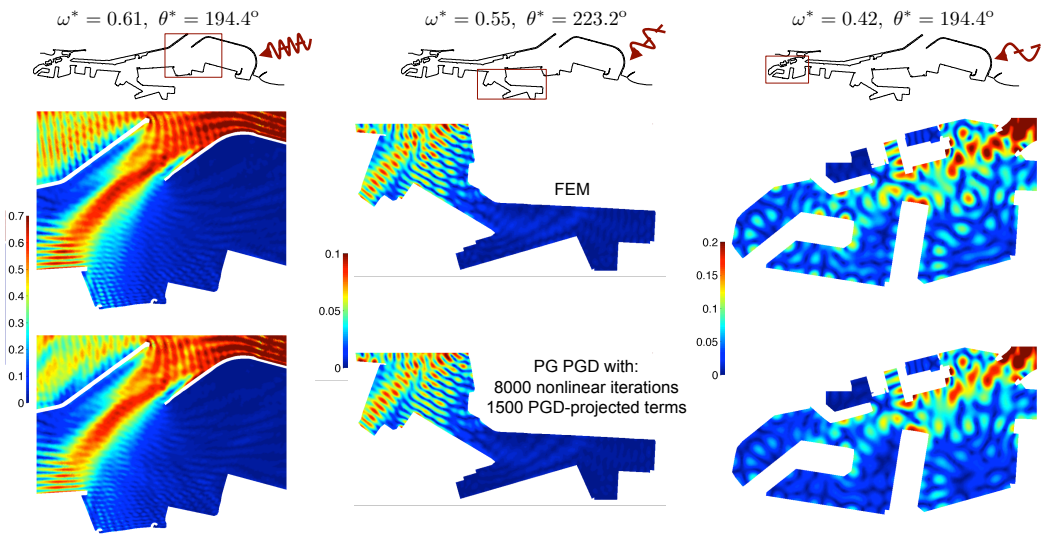

Figure 12: Barcelona harbor: wave-height in different harbor areas (highlighted on top) and values of (ω^*, θ^*): short waves with $(0.61, 1.08\pi)$ (left), mid waves with $(0.55, 1.24\pi)$ (middle) and long waves with $(0.42, 1.08\pi)$ (right). The spatial FEM solution (top) and the PG PGD interpolated solution (bottom) with 1500 PGD-projected terms (8000 solves) are shown.

frequency and incoming wave direction. Particularly, the propagation of sea waves is considered and the harbor agitation study is used as an application example. Each direct computation of the problem involves spatial and parameter dependent coefficients, unbounded physical domains and large reflections induced by the complex geometry. Moreover, the practical applications usually impose numerous direct solutions of this problem for different values of the design parameters.

The non-separability issue of the presented problem is solved using a higher-order PGD-projection: an a posteriori use of the PGD method that separates known multidimensional functions. Formalization of the problem and comparison examples are provided. Results show that optimal expansions (equivalent to those from POD) are obtained when two separated dimensions are used. When the separation is done in more that two dimensions, the PGD-projection can outperform decompositions given by the standard higher-order singular value decomposition (HOSVD). Moreover, the projection of previously computed PGD solutions provides a drastic reduction in the number of terms of the expansion with marginal extra cost. Thus, improvements in memory requirements and online runtime are obtained.

Two different PGD approaches, standard and Petrov-Galerkin ones, are compared. The PG PGD clearly outperforms the standard one, providing faster convergences, and converging where the standard PGD fails. Furthermore, the approach requires only a few nonlinear iterations per term (≤ 3) in the offline PGD constructor.

The PGD provides sufficient accuracy for the two engineering harbor agitation problems shown in the paper. The proposed methodology becomes an excellent alternative when a large number of parameter values are required, which is usual in most of applications, for instance wave resonance studies. In

these cases the wave agitation for multiple and fast queries can be efficiently performed via the numerical techniques presented in this work. However, a high frequency range and a large number of reflections degrade the convergence of algorithms. For more general Helmholtz problems, improvements on the PGD are still needed in such situations if higher accuracy is of concern.

Acknowledgements

This work has been partially supported by the Spanish Ministry of Science and Competitiveness, through grant number CICYT-DPI2011-27778-C02-01/02 and by the Generalitat de Catalunya, grant number 2014-SGR-1471.

8. References

[1] F. Ihlenburg, I. Babuška, Finite element solution of the Helmholtz equation with high wave number Part I: The h-version of the FEM, Comput. Math. Appl. 30 (9) (1995) 9–37.

[2] F. Ihlenburg, I. Babuška, Finite element solution of the Helmholtz equation with high wave number Part II: the h-p version of the FEM, SIAM J. Numer. Anal. 34 (1) (1997) 315–358.

[3] A. Deraemaeker, I. Babuška, P. Bouillard, Dispersion and pollution of the FEM solution for the Helmholtz equation in one, two and three dimensions, Int. J. Numer. Methods Eng. 46 (4) (1999) 471–499.

[4] S. Tsynkov, Numerical solution of problems on unbounded domains. A review, Appl. Numer. Math. 27 (4) (1998) 465–532.

[5] R. Sevilla, S. Fernández-Méndez, A. Huerta, NURBS-Enhanced Finite Element Method (NEFEM), Int. J. Numer. Methods Eng. 76 (1) (2008) 56–83.

[6] R. Sevilla, S. Fernandez-Mendez, A. Huerta, NURBS-Enhanced Finite Element Method (NEFEM) a seamless bridge between CAD and FEM, Arch. Comput. Methods Eng. 18 (4) (2011) 441–484.

[7] F. Chinesta, A. Leygue, F. Bordeu, J. Aguado, E. Cueto, D. Gonzalez, I. Alfaro, A. Ammar, A. Huerta, PGD-Based Computational Vademecum for Efficient Design, Optimization and Control, Arch. Comput. Methods Eng. 20 (1) (2013) 31–59.

[8] A. Barbarulo, P. Ladevèze, H. Riou, L. Kovalevsky, Proper Generalized Decomposition applied to linear acoustic: A new tool for broad band calculation, J. Sound Vib. 333 (11) (2014) 2422–2431.

[9] U. Hetmaniuk, R. Tezaur, C. Farhat, Review and assessment of interpolatory model order reduction methods for frequency response structural dynamics and acoustics problems, Int. J. Numer. Methods Eng. 90 (13) (2012) 1636–1662.

[10] T. Lassila, A. Manzoni, G. Rozza, On the approximation of stability factors for general parametrized partial differential equations with a two-level affine decomposition, ESAIM-Math. Model. Numer. Anal. 46 (6) (2012) 1555–1576.

[11] Y. Chen, J. S. Hesthaven, Y. Maday, J. Rodríguez, X. Zhu, Certified reduced basis method for electromagnetic scattering and radar cross section estimation, Comput. Methods Appl. Mech. Eng. 233-236 (2012) 92–108.

[12] M. Ganesh, J. S. Hesthaven, B. Stamm, A reduced basis method for electromagnetic scattering by multiple particles in three dimensions, J. Comput. Phys. 231 (23) (2012) 7756–7779.

[13] A. Ammar, B. Mokdad, F. Chinesta, R. Keunings, A new family of solvers for some classes of multidimensional partial differential equations encountered in kinetic theory modelling of complex fluids, J. Non-Newtonian Fluid Mech. 139 (2006) 153–176.

[14] A. Ammar, B. Mokdad, F. Chinesta, R. Keunings, A new family of solvers for some classes of multidimensional partial differential equations encountered in kinetic theory modeling of complex fluids. Part II: transient simulation using space-time separated representations, J. Non-Newtonian Fluid Mech. 144 (2007) 98–121.

[15] F. Chinesta, A. Ammar, E. Cueto, Proper generalized decomposition of multiscale models, Int. J. Numer. Methods Eng. 83 (8-9) (2010) 1114–1132.

[16] F. Chinesta, A. Ammar, F. Lemarchand, P. Beauchene, F. Boust, Alleviating mesh constraints: Model reduction, parallel time integration and high resolution homogenization, Comput. Methods Appl. Mech. Eng. 197 (5) (2008) 400–413.

[17] D. González, A. Ammar, F. Chinesta, E. Cueto, Recent advances on the use of separated representations, Int. J. Numer. Methods Eng. 81 (5) (2010) 637–659.

[18] A. Ammar, D. Ryckelynck, F. Chinesta, R. Keunings, On the reduction of kinetic theory models related to finitely extensible dumbbells, J. Non-Newtonian Fluid Mech. 134 (1-3 SPEC. ISS.) (2006) 136–147.

[19] P. Ladevèze, J.-C. Passieux, D. Néron, The latin multiscale computational method and the proper generalized decomposition, Comput. Methods Appl. Mech. Eng. 199 (21-22) (2010) 1287–1296.

[20] A. Nouy, A generalized spectral decomposition technique to solve a class of linear stochastic partial differential equations, Comput. Methods Appl. Mech. Eng. 196 (45–48) (2007) 4521–4537.

[21] A. Nouy, A priori model reduction through proper generalized decomposition for solving time-dependent partial differential equations, Comput. Methods Appl. Mech. Eng. 199 (2010) 1603–1626.

[22] F. Chinesta, P. Ladeveze, E. Cueto, A short review on model order reduction based on proper generalized decomposition, Arch. Comput. Methods Eng. 18 (4) (2011) 395–404.

[23] K. Karhunen, Uber lineare methoden in der wahrscheinlichkeitsrechnung, Ann. Acad. Sci. Fenn. 37 (1946) 1–79.

[24] M. Loève, Probability Theory, 3rd Edition, Van Nostrand Princeton, 1963.

[25] G. Berkooz, P. Holmes, J. L. Lumley, The proper orthogonal decomposition in the analysis of turbulent flows, Annu. Rev. Fluid Mech. 25 (1) (1993) 539–575.

[26] A. K. Noor, J. M. Peters, Reduced basis technique for nonlinear analysis of structures, AIAA J. 18 (4) (1980) 455–462.

[27] A. Vion, R. Sabariego, C. Geuzaine, A model reduction algorithm for solving multiple scattering problems using iterative methods, IEEE Trans. Magn. 47 (5) (2011) 1470–1473.

[28] P. Rouch, P. Ladevèze, The variational theory of complex rays: A predictive tool for medium-frequency vibrations, Comput. Methods Appl. Mech. Eng. 192 (28-30) (2003) 3301–3315.

[29] J. C. W. Berkhoff, Computation of combined refraction-diffraction, in: Proc. 13th Coastal Engineering Conference, Vol. 1, Vancouver, Canada, 1972, pp. 471–490.

[30] M. W. Dingemans, Water wave propagation over uneven bottoms, Vol. 13 of Advanced Series on Ocean Engineering, World Scientific, 1997.

[31] L. Demkowicz, J. Shen, A few new (?) facts about infinite elements, Comput. Methods Appl. Mech. Eng. 195 (29-32) (2006) 3572–3590.

[32] D. Givoli, High-order local non-reflecting boundary conditions: A review, Wave Motion 39 (4) (2004) 319–326.

[33] G. J. Fix, S. P. Marin, Variational methods for underwater acoustic problems, J. Comput. Phys. 28 (2) (1978) 253–270.

[34] D. Givoli, Recent advances in the DtN FE Method, Arch. Comput. Methods Eng. 6 (2) (1999) 71–116.

[35] J.-P. Berenger, A perfectly matched layer for the absorption of electromagnetic waves, J. Comput. Phys. 114 (2) (1994) 185–200.

[36] D. Givoli, Computational absorbing boundaries, in: S. Marburg, B. Nolte (Eds.), Computational Acoustics of Noise Propagation in Fluids, Springer, Berlin, 2008, Ch. 5, pp. 145–166.

[37] C. Michler, L. Demkowlcz, J. Kurtz, D. Pardo, Improving the performance of perfectly matched layers by means of hp-adaptivity, Numer. Meth. Part. Differ. Equ. 23 (4) (2007) 832–858.

[38] U. Basu, A. K. Chopra, Perfectly matched layers for time-harmonic elastodynamics of unbounded domains: Theory and finite-element im-

plementation, Comput. Methods Appl. Mech. Eng. 192 (11-12) (2003) 1337–1375.

[39] I. Singer, E. Turkel, A perfectly matched layer for the Helmholtz equation in a semi-infinite strip, J. Comput. Phys. 201 (2) (2004) 439–465.

[40] E. Demaldent, S. Imperiale, Perfectly matched transmission problem with absorbing layers: Application to anisotropic acoustics in convex polygonal domains, Int. J. Numer. Methods Eng. 96 (11) (2013) 689–711.

[41] A. Bermúdez, L. Hervella-Nieto, A. Prieto, R. Rodríguez, An exact bounded perfectly matched layer for time-harmonic scattering problems, SIAM J. Sci. Comput. 30 (1) (2007) 312–338.

[42] A. Ammar, A. Huerta, F. Chinesta, E. Cueto, A. Leygue, Parametric solutions involving geometry: a step towards efficient shape optimization, Comput. Methods Appl. Mech. Eng. 268 (2014) 178–193.

[43] S. Zlotnik, P. Díez, D. Modesto, A. Huerta, Proper Generalized Decomposition of a geometrically parametrized heat problem with geophysical applications, to appear in Int. J. Numer. Methods Eng.

[44] I. Babuška, F. Ihlenburg, E. Paik, S. Sauter, A Generalized Finite Element Method for solving the Helmholtz equation in two dimensions with minimal pollution, Comput. Methods Appl. Mech. Eng. 128 (3-4) (1995) 325–359.

[45] L. L. Thompson, P. M. Pinsky, Galerkin least-squares finite element method for the two-dimensional Helmholtz equation, Int. J. Numer. Methods Eng. 38 (3) (1995) 371–397.

[46] A. Loula, D. Fernandes, A quasi optimal Petrov-Galerkin method for Helmholtz problem, Int. J. Numer. Methods Eng. 80 (12) (2009) 1595–1622.

[47] G. Giorgiani, D. Modesto, S. Fernández-Méndez, A. Huerta, High-order continuous and discontinuous Galerkin methods for wave problems, Int. J. Numer. Methods Fluids 73 (10) (2013) 883–903.

[48] H. Bériot, G. Gabard, E. Perrey-Debain, Analysis of high-order finite elements for convected wave propagation, Int. J. Numer. Methods Eng. 96 (11) (2013) 665–688.

[49] A. Ammar, F. Chinesta, P. Díez, A. Huerta, An error estimator for separated representations of highly multidimensional models, Comput. Methods Appl. Mech. Eng. 199 (2010) 1872–1880.

[50] T. G. Kolda, B. W. Bader, Tensor decompositions and applications, SIAM Rev. 51 (3) (2009) 455–500.

[51] M. Barrault, Y. Maday, N. C. Nguyen, A. T. Patera, An 'empirical interpolation' method: Application to efficient reduced-basis discretization of partial differential equations, C. R. Math. 339 (9) (2004) 667–672.

[52] F. Collino, P. Monk, Optimizing the perfectly matched layer, Comput. Methods Appl. Mech. Eng. 164 (1–2) (1998) 157–171.

[53] D. Rabinovich, D. Givoli, E. Bécache, Comparison of High-Order Absorbing Boundary Conditions and Perfectly Matched Layers in the Frequency Domain, Int. J. Numer. Meth. Biomed. 26 (10) (2010) 1351–1369.

[54] L. De Lathauwer, B. De Moor, J. Vandewalle, A multilinear singular

value decomposition, SIAM J. Matrix Anal. Appl. 21 (4) (2000) 1253–1278.

[55] J. D. Carroll, J.-J. Chang, Analysis of individual differences in multidimensional scaling via an n-way generalization of "Eckart-Young" decomposition, Psychometrika 35 (3) (1970) 283–319.

[56] R. A. Harshman, Foundations of the PARAFAC procedure: Models and conditions for an "explanatory" multimodal factor analysis, UCLA working papers in phonetics 16 (1970) 1–84.

[57] D. Amsallem, C. Farhat, Interpolation method for adapting reduced-order models and application to aeroelasticity, AIAA J. 46 (7) (2008) 1803–1813.

[58] C. A. Andersson, R. Bro, The N-way Toolbox for MATLAB, Chemom. Intell. Lab. Syst. 52 (1) (2000) 1–4.

[59] T. H. Fay, The butterfly curve, Am. Math. Mon. 96 (5) (1989) pp. 442–443.

Appendix A. The higher-order PGD-projection

This Appendix introduces a method that uses the PGD rationale to obtain separable approximations of known functions. Similarly to higher-order SVD [54] or the so-called CANDECOMP/PARAFAC (CP) methods [55, 56], this approach is designed to compute separable multidimensional functions. For a comprehensive review in HOSVD and CP methods see [50]. Due to this analogy, the proposed technique is coined as *higher-order PGD-projection*. The PGD-projection generally produces separable representations with less

terms compared with HOSVD. Moreover, the projection does not require the a priori selection of the number of terms for the separated solution (as CP does).

Consider a known d-dimensional function $f(z_1, \ldots, z_d)$ with coordinates $z_i \in \Omega_i$ for $i = 1, \ldots, d$, which can be evaluated at any point of the high-dimensional domain $\Omega = \Omega_1 \times \cdots \times \Omega_d$. A rank-$n$ PGD approximation of f is defined as

$$\begin{aligned} f_\pi^n(z_1, \ldots, z_d) = \boldsymbol{\pi}^{\texttt{pgd}}\big[f(z_1, \ldots, z_d)\big] &= \sum_{m=1}^{n} \beta^m \prod_{i=1}^{d} F_{\pi,i}^m(z_i). \\ &= f_\pi^{n-1}(z_1, \ldots, z_d) + \beta^n \prod_{i=1}^{d} F_{\pi,i}(z_i). \end{aligned} \tag{A.1}$$

The coefficients β^m are determined by a $\mathcal{L}^2$ projection once all $F_{\pi,i}^m$ are known (note that they are normalized, i.e. $\big\|F_{\pi,i}^m\big\|_{\Omega_i} = 1$ for $m = 1, \ldots, n$ and $i = 1, \ldots, d$). This implies solving the typical symmetric and dense system of normal equations

$$\sum_{m=1}^{n} \big(\psi_s, \psi_m\big)_\Omega \, \beta^m = \big(\psi_s, f\big)_\Omega \text{ for all } s = 1, \ldots, n$$

with $\psi_s = \prod_{i=1}^{d} F_{\pi,i}^s$. While the rhs requires to integrate over the d-dimensional domain, the coefficients of the lhs matrix are simply products of 1D integrals, that is

$$\big(\psi_s, \psi_m\big)_\Omega = \prod_{i=1}^{d} \big(F_{\pi,i}^s, F_{\pi,i}^m\big)_{\Omega_i}.$$

The greedy algorithm described in Section 4.1 with an alternating direction approach is used to compute functions $F_{\pi,i}^m$ for $m = 1, \ldots, n$ and $i = 1, \ldots, d$. This strategy pursues finding the separable approximation defined by (A.1) that minimizes the $\mathcal{L}^2$ distance between f_π^n and f. However, as it will be explained later, it only guarantees to find the optimum when

separating two dimensions. Each term ("mode") is obtained with the $\mathcal{L}^2$ projection on the tangent space, namely

$$\left(\delta f, \prod_{i=1}^{d} F_{\pi,i}\right)_\Omega = \left(\delta f,\ f - f_\pi^{n-1}\right)_\Omega \tag{A.2}$$

with test functions in the tangent space

$$\delta f = \delta F_{\pi,1} F_{\pi,2} \cdots F_{\pi,d} + F_{\pi,1} \delta F_{\pi,2} \cdots F_{\pi,d} + \cdots + F_{\pi,1} \cdots F_{\pi,d-1} \delta F_{\pi,d}, \tag{A.3}$$

and then normalized.

The following examples show the behavior and properties of the PGD-projection. When the separation involves two dimensions only, the PGD-projection minimizes the L2 distance in the same way POD does. The two separation procedures are therefore identical in that case and the separated solution obtained by PGD is optimal. This result coincides with [21]. Note however, that, in contrast with POD, the PGD-projection does not requires the solution of a SVD problem. Moreover, with PGD the approximation space for the separated representation is taken into account during the minimization process. Consequently, there is no need for extra interpolation techniques at those values outside the snapshots space, see for instance [57]. Furthermore, PGD has the advantage of a straightforward generalization to higher dimensions. There is no need for special implementations such as in HOSVD, and in the tested examples, PGD produces lower rank solution compared to HOSVD to obtain a given accuracy.

Finally, a practical use of the PGD-projection concerns the compression (reduction in the number of terms) of an already separated function f. This process is extremely fast when implementing the PGD-projection. The rhs of (A.2), when f is separable, is computed as products of 1D integrals as discussed in Section 5, therefore this compression is fast to perform. Furthermore, these integrals are all $\mathcal{L}^2$-projections on both sides of Eq. (A.2),

implying that the computation of $F_{\pi,i}$ for $i = 1, \ldots, d$ is performed by solving a diagonal linear system. The efficiency of the algorithm is therefore drastically improved.

These properties are shown next using three different examples. All the PGD-projections are computed with a maximum number of 5 iterations per term. For comparison purposes, the HOSVD is also computed in the last example using the extended N-way package for tensor decomposition in MATLAB® [58].

Appendix A.1. Reproducing a function in separated representation

A function, which has a separated representation, $f(x, y)$ with $(x, y) \in [0, 1]^2$ is considered first. It consists in the product of two 1D polynomials, namely $P_q(x)$ and $P_s(y)$, defined by

$$f(x, y) = P_q(x)P_s(y) = \sum_{i=0}^{q} x^i \sum_{j=0}^{s} y^j = 1 + x + y + xy + \cdots + x^q y^s. \quad \text{(A.4)}$$

Note that the actual rank of this function is one. Therefore the PGD-projection, namely

$$f_\pi^n(x, y) = \boldsymbol{\pi}^{\texttt{pgd}}\big[f(x, y)\big] = \sum_{m=1}^{n} \beta^m F_{\pi,1}^m(x) F_{\pi,2}^m(y), \quad \text{(A.5)}$$

must separate the function f with only one term ($n = 1$) independently of the order of the polynomials, i.e. q and s. Since the PGD algorithm normalizes the separated functions $F_{\pi,2}^1$ and $F_{\pi,2}^1$, the projection must provide these functions as $F_{\pi,1}^1 = P_q / \|P_q\|$, $F_{\pi,2}^1 = P_s / \|P_s\|$, and the coefficient as $\beta^1 = \|P_q\| \, \|P_s\|$. Relative errors below 10^{-15} are obtained in these three expressions when solving for (A.5) using 100 nodes to discretize the 1D domains.

PGD-projection properties can be additionally explored by means of a modification of the function (A.4), namely $\tilde{f}$. More precisely, only the major

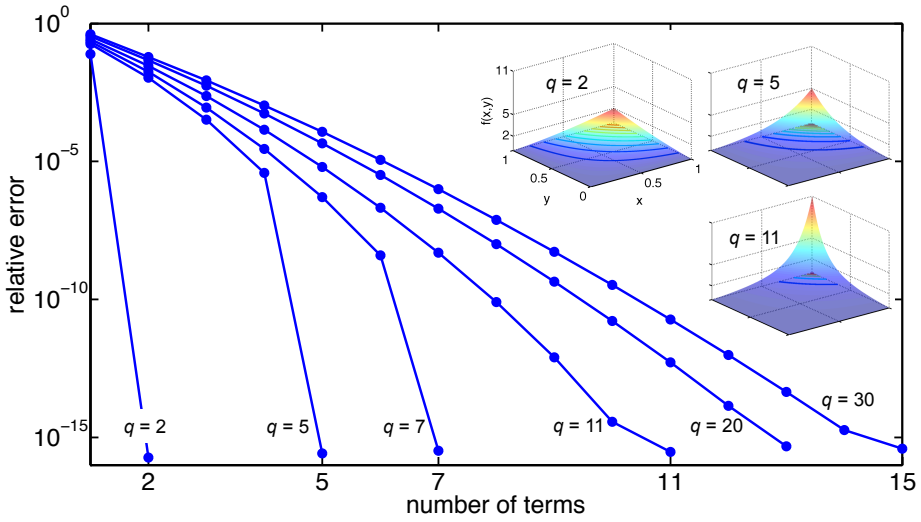

Figure A.13: Separable function: convergence of the $\mathcal{L}^2$ relative error of the PGD-projected function $\tilde{f}_\pi^n$. The value q denotes the number of terms of the exact function. This function is depicted for the cases $q = \{2, 5, 11\}$.

order products in the expansion are taken into account, that is

$$\tilde{f}(x, y) = \sum_{i=0}^{q} x^i \, y^i = 1 + xy + x^2 y^2 + \cdots + x^q y^q. \tag{A.6}$$

Note that this function is no longer rank one for $q > 1$. Figure A.13 shows the relative error of the PGD-projected function $\tilde{f}_\pi^n$, depicted with respect to the number of projected terms (n). Different values of q in Eq. (A.6) are studied. The exact function $\tilde{f}$ particularized for the cases $q = \{2, 5, 11\}$ is also shown.

Results demonstrate that PGD-projection is able to capture the separability of the function $\tilde{f}$: the number of terms required to reproduce the function (n) is, as maximum, exactly to the number of terms provided (q). Moreover, the PGD-projection leads to compressed expansions for $q > 11$, that is, it provides $n << q$ terms that perfectly capture the function $\tilde{f}$. This is produced because the difference between the last terms of $\tilde{f}$ is small, for

large values of q, and for points in $[0,1]^2$.

Appendix A.2. Planar waves

The separability of two planar waves are studied next. The functions to be approximated are

$$f_1(x,k,\theta) = \exp(ikx\cos\theta), \quad f_2(x,k,\theta) = \exp(ikx\sin\theta),$$

with $i = \sqrt{-1}$. The two PGD-projections imposed here separate x from (k,θ), for instance for the function f_1 that is

$$f_{\pi,1}^{n_1}(x,k,\theta) = \pi^{\texttt{pgd}}\big[f_1(x,k,\theta)\big] = \sum_{m=1}^{n_1} \beta^m F_{\pi,1}^m(x) F_{\pi,2}^m(k,\theta),$$

and analogously for the function f_2 and its projection $f_{\pi,2}^{n_2}$. Thus, two separated functions are used and the PGD-projection can be compared with POD using a standard SVD. The spatial coordinate is defined in a unitary domain, $x \in [0,1]$, while $(k,\theta) \in [1,600]\times[\pi,2\pi]$. Thus, the number of waves in the spatial domain range from 1 (low-frequency) to 95 (high-frequency). Along each dimension a discretization with $500\times100\times100$ nodes for (x,k,θ) is used.

Convergence of the normalized coefficients for both functions f_1 and f_2 are shown in Figure A.14. For high fidelity purposes (normalized coefficients below 10^{-8}), over 200 terms are necessary when projecting f_1 while 100 are obtained in the projection of f_2. The coefficients of the SVD are also depicted in Figure A.14 for comparison purposes.

Results clearly show that the PGD-projection provide optimal expansions in this case. That is, the greedy procedure is able to find the optimal decomposition that minimizes the distance between f_i and $f_{\pi,i}^{n_i}$, $i = \{1,2\}$, in the $\mathcal{L}^2$ norm. Moreover, every in example tested in two dimensions (i.e. separated representations with sums of products of two functions) the PGD-projection coincides with the SVD method.

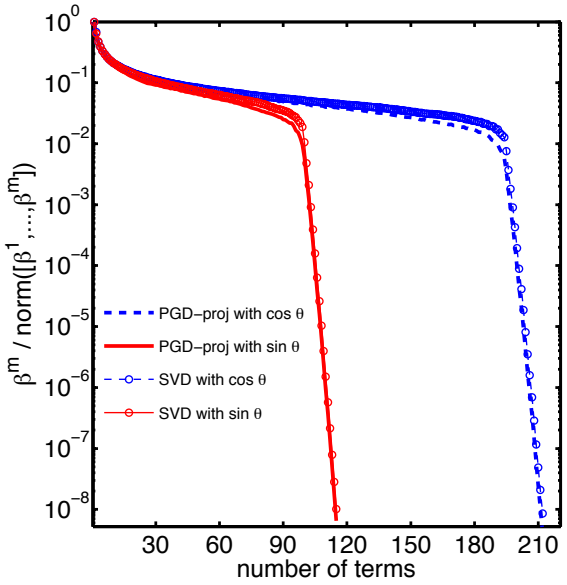

Figure A.14: Planar waves: normalized coefficients for the PGD-projection and the SVD vs. number of terms. Exact functions are $f_1 = \exp(ikx\cos\theta)$ (blue line) and $f_2 = \exp(ikx\sin\theta)$ (red line).

Appendix A.3. The butterfly curve

This last test uses a highly non-separable 6D function based on the family of "butterfly curves", see [59], that is

$$f(\theta, a, b, c, d, e) = a\exp(\cos\theta) - b\cos(c\,\theta) + \sin^d(\theta/e),$$

with $\theta \in [0, 2\pi]$, $a \in [-1, 1]$, $b \in [-3, 3]$, $c \in [0, 4]$, $d \in [0, 5]$ and $e \in [1, 12]$.

The PGD-projection must seek an approximation in the following form:

$$f_\pi^n(\theta, a, b, c, d, e) = \sum_{m=1}^{n} \beta^m F_{\pi,1}^m(\theta) F_{\pi,2}^m(a) F_{\pi,3}^m(b) F_{\pi,4}^m(c) F_{\pi,5}^m(d) F_{\pi,6}^m(e). \quad \text{(A.7)}$$

Discretized 6D domain uses 100 nodes along dimension θ, whereas 20 nodes are used for the rest of dimensions but the parameter d, that uses 6 equally spaced nodes.

The higher-order approach provided by the standard HOSVD is also computed in this example. Using a similar notation as in Eq. (A.7), the HOSVD

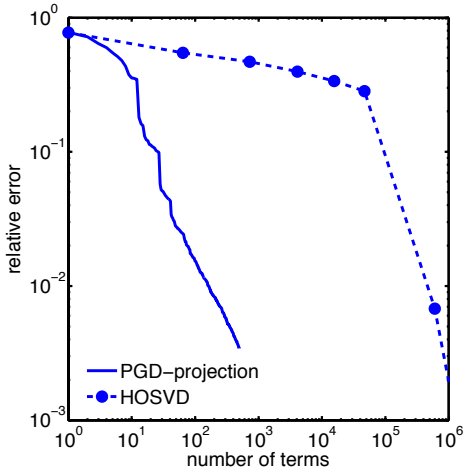

Figure A.15: Butterfly curve: relative error of the PGD-projection (solid line) and the $(n_1, n_2, \ldots, n_6)$ HOSVD (dashed line). Markers on the HOSVD curve represent those cases where $n_1 = n_2 = \cdots = n_6$.

approximation of the function f writes

$$f_{\texttt{hosvd}}^{(n_1,n_2,\ldots,n_6)}(\theta, a, \ldots, e) = \sum_{i=1}^{n_1}\sum_{j=1}^{n_2}\cdots\sum_{l=1}^{n_6}\beta^{ij\ldots l}F_1^i(\theta)F_2^j(a)\cdots F_6^l(e).$$

The evaluation of $f_{\texttt{hosvd}}^{(n_1,n_2,\ldots,n_6)}$ is done by means of tensor decomposition methods, see [50] for details. Note that, for practical purposes, comparison between PGD-projection and HOSVD requires comparing the number of PGD terms (n), and the number of HOSVD terms $(n_1 n_2 \cdots n_6)$.

Relative errors of f_π^n and $f_{\texttt{hosvd}}^{(n_1,n_2,\ldots,n_6)}$ are depicted in Figure A.15. These errors are measured with the $\mathcal{L}^2$ norm of the difference between f and both approximations. The often suggested choice $n_1 = n_2 = \cdots = n_6$ is used for the HOSVD, notwithstanding that other combinations have been also explored with no significant changes in the results. The PGD-projection clearly outperforms the HOSVD, requiring three orders of magnitude less terms to reach the same level of accuracy. The Figure A.16 illustrates this conclusion particularizing three polar plots of the curve $f^*(\theta) = f(\theta, a^*, \ldots, e^*)$

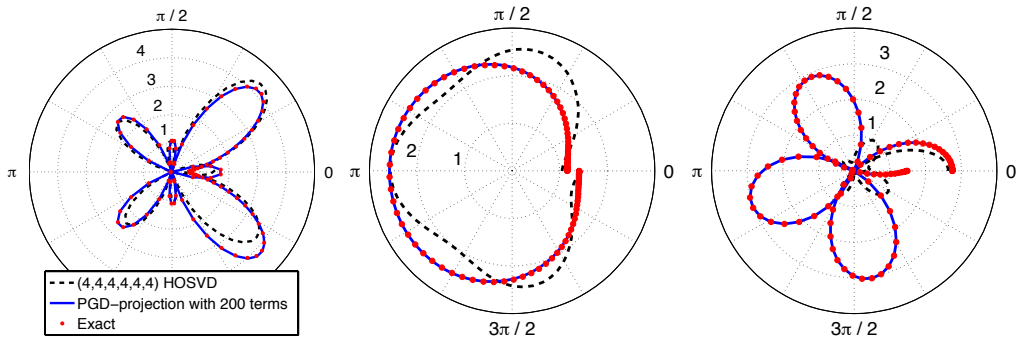

Figure A.16: Butterfly curve: polar plots of $f(\theta, a^*, \ldots, e^*)$ for fixed values $a^*, b^*, \ldots, e^*$. Approximations given by the PGD-projection (solid line) and the HOSVD (dashed line) are shown. Values of $a^* = 1$, $b^* = 2.1213$, $c^* = 4$, $d^* = 5$, $e^* = 12$ (left), $a^* = -0.5736$, $b^* = -2.7189$, $c^* = 0$, $d^* = 2$, $e^* = 11.9791$ (center), and $a^* = -0.0872$, $b^* = -2.9886$, $c^* = 1.8257$, $d^* = 3$, $e^* = 7.9235$ (right).

for different fixed values $a^*, b^*, \ldots, e^*$ of the parametric dimensions. Note that abrupt changes in the curve shape between the three cases indicate the highly nonlinear behavior of the exact function f. The PGD-projection with 200 terms satisfactory captures the exact values for all the cases, while on the contrary the approximation $f_{\texttt{hosvd}}^{(4,4,\ldots,4)}$, that provides 20 times more terms, does not exhibit acceptable results specially for the last case.